optica

Video-rate large-scale imaging with Multi-Z confocal microscopy: supplementary material

AMAURY BADON[1*], SETH BENSUSSEN[1], HOWARD J. GRITTON[1], MEHRAJ R. AWAL[2], CHRISTOPHER V. GABEL[2,3], XUE HAN[1,3], AND JEROME MERTZ[1,3]

[1] Department of Biomedical Engineering, Boston University, Boston, Massachusetts 02215, USA
[2] Department of Physiology and Biophysics, Boston University School of Medicine, Boston, Massachusetts 02218, USA
[3] Boston University Photonics Center, Boston, Massachusetts 02215, USA
[*] Corresponding author: abadon@bu.edu

Published 21 March 2019

This document provides supplementary information to "Video-rate large-scale imaging with Multi-Z confocal microscopy," https://doi.org/10.1364/OPTICA.6.000389. It provides details related to the experimental setup, optical sectioning, point spread function simulations, high resolution volumetric imaging, screening of the reflective pinholes and crosstalk between the different detection channels.

1. DETAILS ON EXPERIMENTAL SETUP

Our experimental setup consists of a standard confocal microscope with tube lens L_1 (f=500 mm) and scan lens L_2 (f=100 mm), and allows easy switching from a 10× to a 20× microscope objective (see Fig. S1). To maintain a constant magnification from sample to pinhole ($M = 62.5$), a 4f system comprised of lenses L_3 (f=150 mm) and L_4 (f=150 mm) is simply replaced by L_3' (f=100 mm) and L_4' (f=200 mm). Since the sum of the focal lengths of the relay lenses remains the same in both configurations, no further modification is necessary.

An optional electric tunable lens (ETL) is positioned between the dichromatic mirror and the scanning unit. In this manner, the induced axial shift in the focal plane of the MO is cancelled upon the return of the fluorescence through the detection path. Since the ETL is close to a pupil plane (here the scanning mirrors), we can shift the focus without significantly modifying the total magnification and resolution of the system [1]. The ETL is controlled using a serial connection and a National Instruments DAQ board. A custom Matlab script that controls both ScanImage and the voltage applied to the ETL enables the acquisition of interleaved frames.

2. OPTICAL SECTIONING CAPACITY OF MULTI-Z CONFOCAL MICROSCOPY

To estimate the optical sectioning capacity of our microscope, we measured the signals from a thin fluorescent plane recorded by each channel at different z positions of a motorized stage. For each channel we obtained axial full widths at half maximum of 48.2, 50.6, 45.6 and 47.3 μm from the deepest to shallowest depths respectively (see Fig. S2).

3. POINT SPREAD FUNCTION SIMULATIONS

The system point spread function denoted by $\mathrm{PSF}_{\mathrm{conf}}$ is given by the product of the illumination point spread function $\mathrm{PSF}_{\mathrm{i}}$ and the detection point spread function $\mathrm{PSF}_{\mathrm{d}}$ convolved with the pinhole function A_{p} (projected into the sample). This is given by

$$\mathrm{PSF}_{conf}(\boldsymbol{\rho}, z, z_D) = \mathrm{PSF}_i(\boldsymbol{\rho}, z) \times \int\int A_p(\boldsymbol{\rho}')\mathrm{PSF}_d(\boldsymbol{\rho}' - \boldsymbol{\rho}, z - z_D)d^2\boldsymbol{\rho}' \tag{S1}$$

where $\boldsymbol{\rho}$ and z are transverse and axial coordinates respectively, and z_D is the axial shift of the object plane of interest.

The 3D illumination point spread function is modeled by a Gaussian-Lorentzian profile [2]:

$$\mathrm{PSF}_i(\boldsymbol{\rho}, z) = \frac{1}{\pi w_0^2(1+\xi^2)} e^{-2\rho^2/w_0^2(1+\xi^2)} \tag{S2}$$

where w_0 is the beam waist and

$$\xi = \frac{z}{4\kappa\pi w_0^2} \tag{S3}$$

where κ is the wavenumber.

The 3D detection point spread function is modeled using the paraxial approximation [2], assuming the MO pupil is circular and unobstructed.

The results shown in Fig. S3 are obtained using a MO numerical aperture $\mathrm{NA}_d = 0.45$, a pinhole diameter d=4.8 μm (in the sample plane), z_D=-37.5, -12.5, +12.5 and +37.5 μm corresponding to the positions of the four reflecting pinholes, and an illumination beam waist w_0=1.75 μm. While we have neglected aberrations in these simulations, both the peak value and the

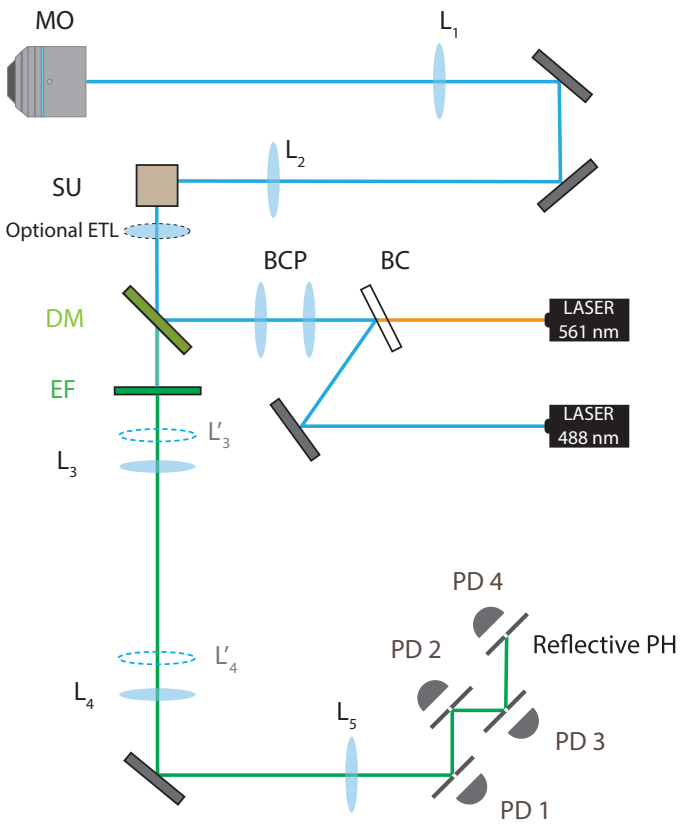

Fig. S1. BC: beam combiner, BCP: beam compressor, DM: dichromatic mirror, EF emission filter, ETL: electric tunable lens, SU: scanning unit, MO: microscope objective, L: lens and PD: photodetector.

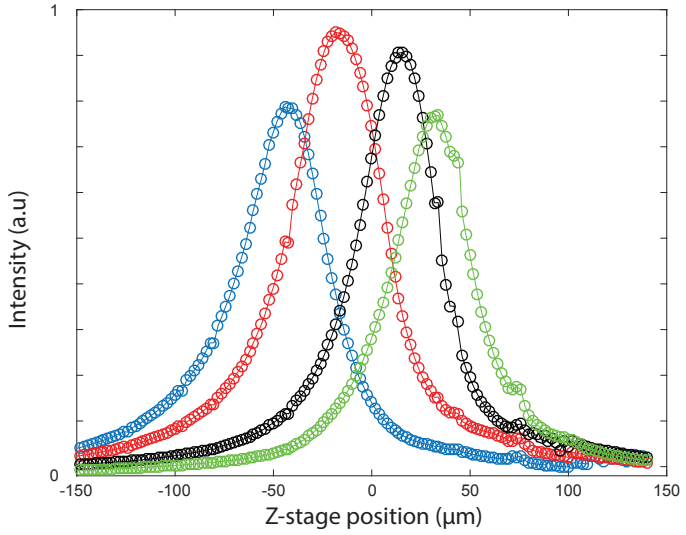

Fig. S2. Optical sectioning capacity of the Multi-Z confocal microscope. Signals from a thin fluorescent plane recorded by the four channels. The fluorescent plane was axially scanned using a motorized Z-stage.

axial extent of the responses for the four different channels are in rough agreement with the experimental results, suggesting that aberrations did not play a major role over an axial range on the order of 100 microns. Note that we can define an equivalent illumination NA for the Gaussian beam from the circular area in the pupil plane that encompasses 90% of the total power, leading to an equivalent illumination NA in our case of about 0.12.

Finally we show in figure S3f the theoretical transverse profile of the system PSF for two different channels. From this, we observe that the pinhole diameter amply spans the transverse extent of the detected intensity, with 97% and 98% of the total signal power being detected for the imaging planes at -12.5 and -37.5 μm respectively.

4. COMPARISON BETWEEN MULTI-Z AND CONVENTIONAL CONFOCAL MICROSCOPY

To further compare the performances of our Multi-Z approach with more conventional confocal microscopy, we present in Fig. S4 a side-by-side comparison of a 4-plane image acquired simultaneously by Multi-Z our microscope, and approximately the same 4 planes acquired sequentially by moving the sample stage along Z and using data only from the second pinhole (since this provided the best transverse and axial resolutions). Similar performances are obtained when comparing with the other pinholes.

5. CROSSTALK AND PINHOLE SCREENING

The multiple image planes acquired by our system are not wholly independent, and we analyze here their degree of interaction.

First, we observe from Figs. 1d and S3g that there is overlap in the axial profiles of the PSFs associated with each image plane, even for point-object samples. This overlap leads to crosstalk between different channels. In other words, an object in one plane may appear in another, though with a different intensity weight. The degree of crosstalk depends on the degree of overlap between PSFs, which, in turn, depends on their separation ΔZ and on the extent of their axial responses. These are user controlled parameters. In other words, the crosstalk can be tuned to be high or low depending on experimental requirements. A high crosstalk may be preferred to minimize gaps between image planes and prioritize a roughly uniform detection efficiency along the excitation axial profile. The different intensity weights recorded in each channel can even be used, in principle, to enable high-accuracy axial localization, using a technique described in [3]. Alternatively, a low crosstalk may be preferred to prioritize independence between image planes. For example, crosstalk can be reduced by extending ΔZ (e.g. by increasing the distance between pinholes or by decreasing magnification M), or by compressing the PSF_d axial range (e.g. by decreasing pinhole size or increasing detection NA).

The degree of crosstalk can be characterized by the (axially-integrated) proportion of each PSF that is associated with each image plane. In our case, the two central imaging planes are defined as depths comprised between -25 and 0 μm, and 0 and +25 μm respectively. The low and high integration limits for the leftmost and rightmost imaging planes, respectively, were extended to infinity. Based on fits of the experimental PSFs shown in Figure 1, we obtain the crosstalk matrix:

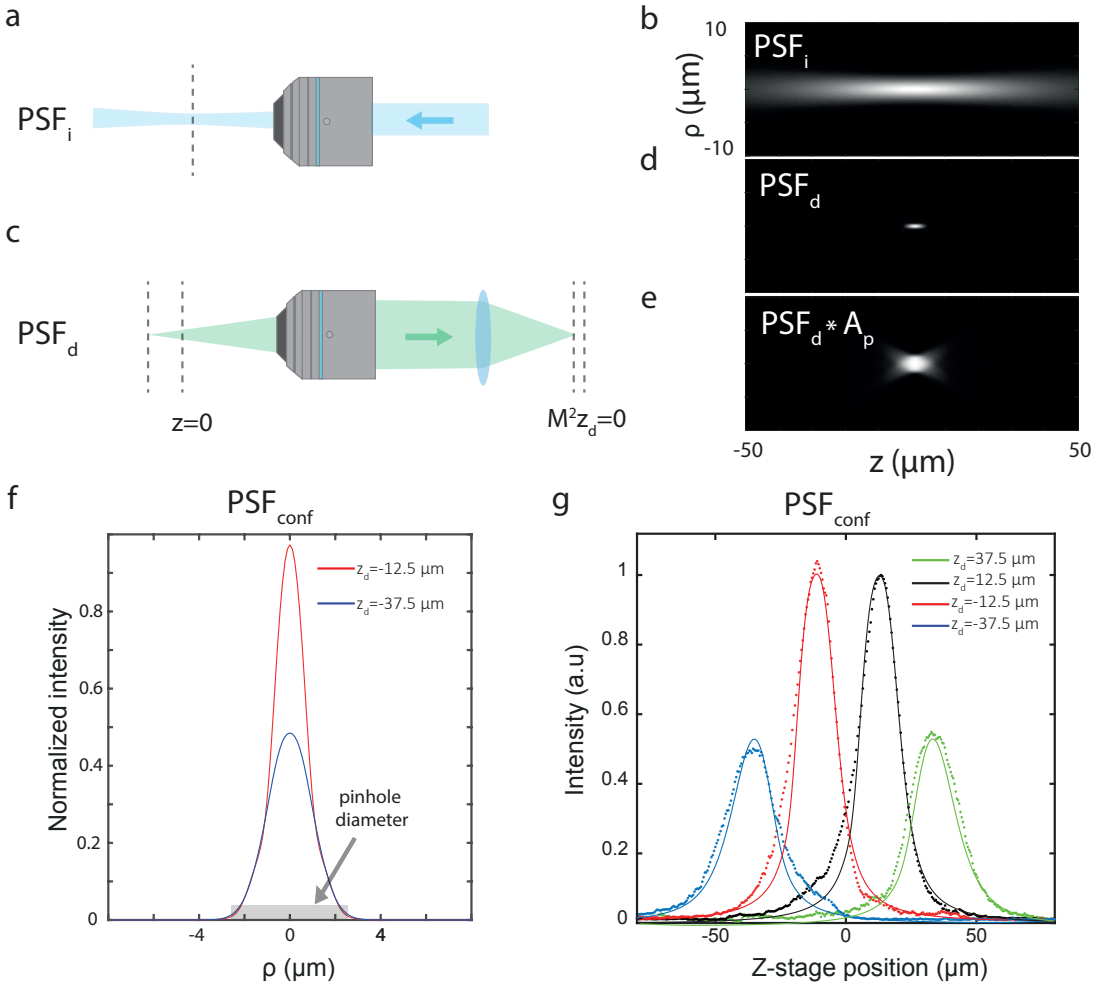

Fig. S3. (a) Schematic of the low-NA illumination and corresponding theoretical point spread function (b). (c) Schematic of the high-NA detection and corresponding theoretical point spread function (d). (e) Theoretical detection point spread function convolved with the pinhole function. (f) Theoretical transverse point spread function for channels associated with imaging planes at depths -12.5 and -37.5 μm. (g) Theoretical sub-diffraction bead intensity detected by each of the four channels (continuous lines) and comparison with experiment (dashed lines).

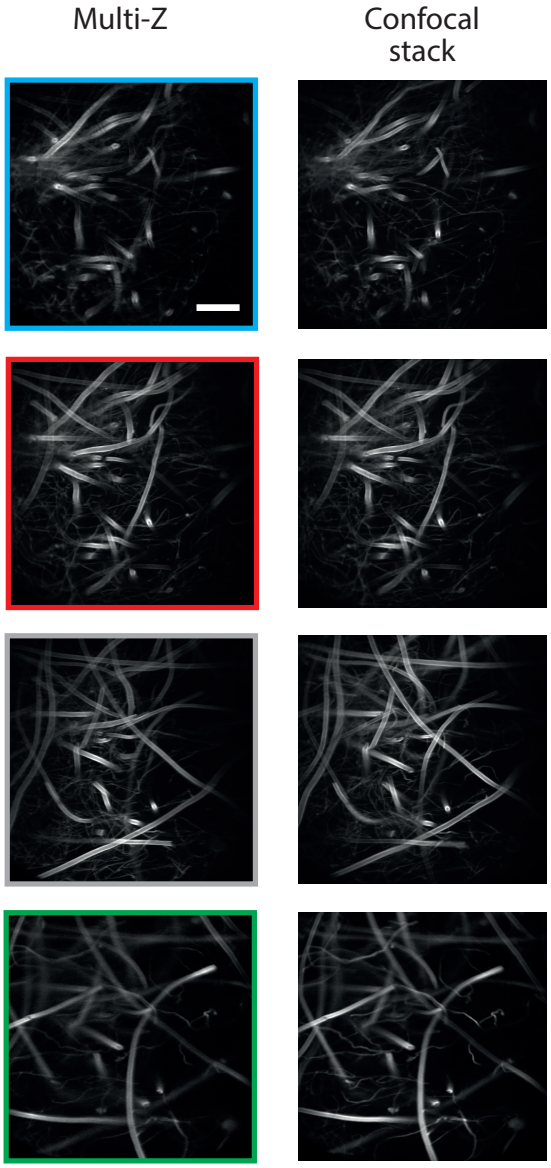

Fig. S4. Side-by-side comparison a Multi-Z stack (left column) and the same stack acquired sequentially using data only from pinhole 2 (right column). The sample is a fixed Aspergillus Conidiophores. Scale bar, 200 μm.

	Ch 1	Ch 2	Ch 3	Ch 4
Ch 1	79	15	4	2
Ch 2	9.5	79	9.5	2
Ch 3	2	9.5	79	9.5
Ch 2	2	4	15	79

We emphasize that this crosstalk matrix is not related to our use of multiple reflecting pinholes, and the same result would be obtained if each image plane were measured separately with a single pinhole.

On the other hand, the presence of multiple reflecting pinholes leads to a second interaction between image planes, referred to here as pinhole screening. Specifically, the light that would normally propagate to a given pinhole can be partially shunted by the presence of upstream pinholes. This shunting effect is dominated by the nearest upstream pinhole, and is absent, of course, for the first pinhole (corresponding to the deepest imaging plane). In practice, this effect is small, and the pinhole screening amounts to no more than 4% in our case, for the last three pinholes only.

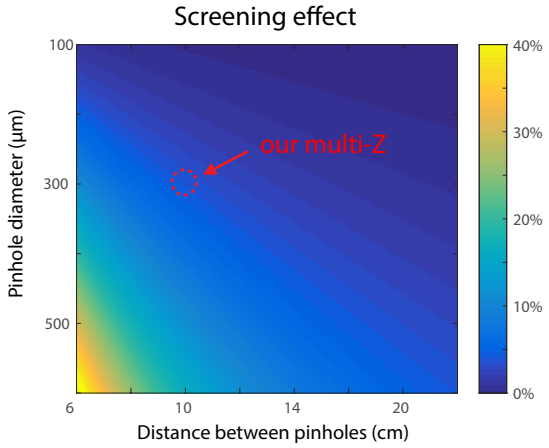

Fig. S5. Influence of the pinhole diameter and distance between two consecutive pinholes on the screening effect.

As expected, this amount of screening mainly depends on the diameter of the pinhole and the physical distance between consecutive reflecting pinholes. Figure S5 displays the effect of these parameters on the amount of screening, while maintaining constant all the other microscope parameters (magnification, numerical aperture, etc.).

6. INFLUENCE OF THE PINHOLE DIAMETER ON RESOLUTION

For the configuration presented in this work, we purposefully compromised our transverse resolution to allow axially elongated illumination and enable video-rate acquisition over a large FOV. Depending on the application of interest, other configurations could be envisaged that prioritize different imaging parameters (axial or transverse resolution, axial range, number of planes, crosstalk, etc.). Here, we focus on the effect of the pinhole diameter on the transverse and axial resolutions, which in turn affect optical sectioning. We consider the case where we fix the number of channels (4), the NA for the detection (NA$=$ 0.45) and the inter-plane distance ΔZ. Figure S6 displays the dependence of the transverse and axial full widths at half maximum of the probe volume associated with one channel as a function of the pinhole diameter. As the axial range of Multi-Z is mainly limited by the illumination beam profile, we compare the performances for different illumination NA's, here 0.05, 0.1 and 0.2. The results were obtained using Eq. S1 and the pinhole diameter is given in Airy units (AU) associated with the detection aperture:

$$1\ AU = \frac{1.21\lambda}{NA_d} \tag{S4}$$

7. LOCATION OF THE DETECTED NEURONS

To demonstrate the ability of Multi-Z to detect independent neurons from different depths, we display the locations of the neurons identified at each plane by the CNMF algorithm and

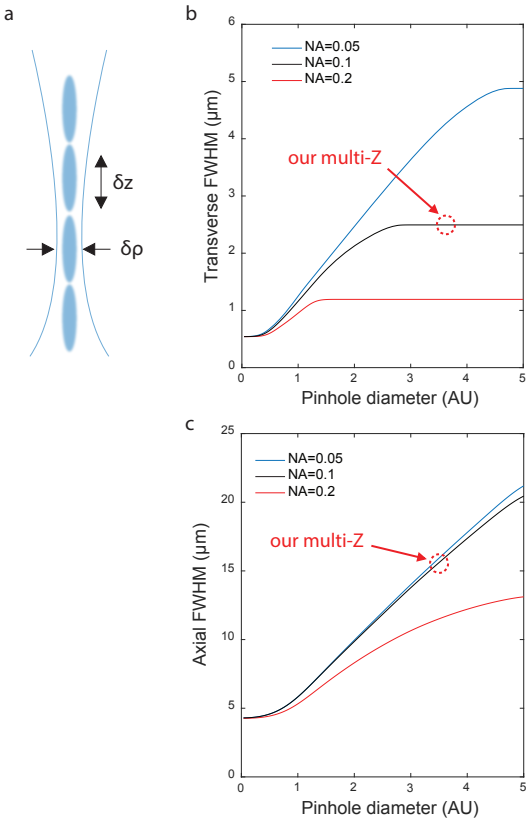

Fig. S6. Performance of Multi-Z confocal microscopy as a function of the pinhole diameter. (a) Schematic of the illumination beam profile and different probe volumes. (b) Transverse full width at half maximum as a function of the pinhole diameter for illumination NA equal to 0.05, 0.1 and 0.2. (c) Axial full width at half maximum as a function of the pinhole diameter for illumination NA equal to 0.05, 0.1 and 0.2.

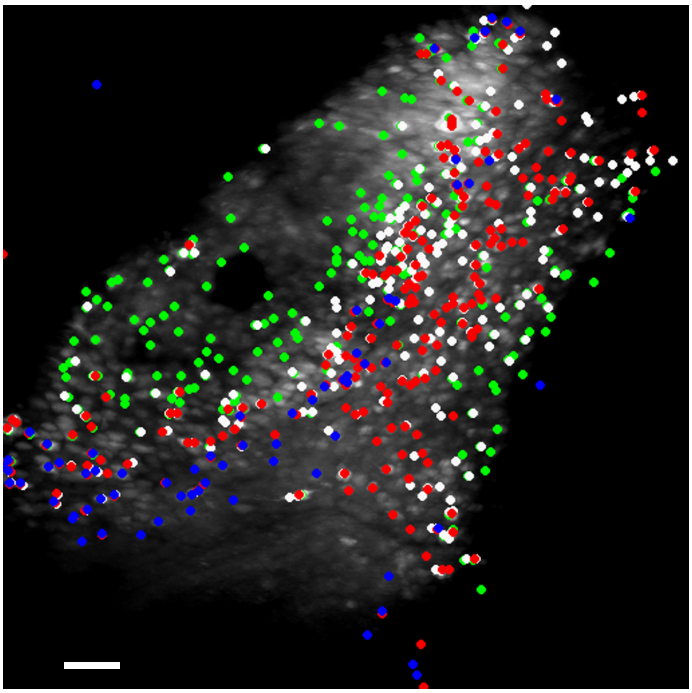

Fig. S7. Locations of the identified neurons superimposed onto the extended-depth-of-field image averaged over 20 s. Blue, red, white and green are associated with imaging depths of -37.5, -12.5, +12.5 and +37.5 μm, respectively.

superimpose this onto the extended-depth-of-field image of the mouse brain presented in Section 3.B. Here, the extended-depth-of-field image is averaged over 20 s and the blue, red, white and green dots are associated with imaging depths of -37.5, -12.5, +12.5 and +37.5 μm, respectively. As is apparent in Fig. S7, while some regions of the FOV are associated with different imaging depths due to the curvature of the brain, other regions reveal axially distributed neurons that are detected by the different Multi-Z channels.

REFERENCES

1. B. F. Grewe, F. F. Voigt, M. van t Hoff, and F. Helmchen, "Fast two-layer two-photon imaging of neuronal cell populations using an electrically tunable lens," Biomed. optics express **2**, 2035–2046 (2011).
2. J. Mertz, *Introduction to Optical Microscopy* (Roberts and Company, 2010).
3. J. Tan and F. Wang, "Theoretical analysis and property study of optical focus detection based on differential confocal microscopy," Meas. Sci. Technol. **13**, 1289 (2002).